Primer on Mølmer-Sørensen Gates in Trapped Ions

C. Monroe

June 4, 2020

Abstract

The most advanced physical system for quantum bits or effective spins is a collection of trapped atomic ions. This is evidenced by the number of controlled and interacting qubits, the quality of quantum gates and interactions, and the fidelity of initialization/measurement fidelities. Trapped atomic ions, held in a vacuum chamber and confined away from surfaces or solids by electromagnetic fields, laser cooled to be nearly at rest and "wired" together with external laser or microwave fields, offer a very clean quantum system to perform quantum computations and simulations. These notes are a primer on the control and entanglement of trapped ion qubits through classical (optical) electromagnetic fields. Special attention is paid to how the control phases are relayed to the qubits.

1 Introduction

1.1 Atomic Ion Qubits

We represent qubits or spins by a crystal of electromagnetically trapped atomic ions, with two electronic energy levels within each ion behaving as an effective qubit or spin-1/2 particle. The particular choice of electronic levels depends on the atomic element and also the desired type of control fields used to manipulate and measure the qubit state. The most important features of these qubit states for executing quantum information processing are (a) the levels are long-lived and exhibit excellent coherence properties, (b) the levels states have appropriate strong optical transitions to auxiliary excited states, allowing for qubit initialization through optical pumping and qubit detection through fluorescence, and (c) the qubits interact through a coherent coupling that can be externally controlled and gated. This restricts the atomic species to a handful of elements and qubit/spin states that are encoded in either $S_{1/2}$ hyperfine or Zeeman ground states of single outer-electron atoms (e.g., Be^+, Mg^+, Ca^+, Sr^+, Ba^+, Cd^+, Zn^+, Hg^+, Yb^+) with radiofrequency/microwave frequency splittings or ground and D or F metastable electronic excited states of single or dual outer-electron atoms (e.g., Ca^+, Sr^+, Ba^+, Yb^+, B^+, Al^+, Ga^+, In^+, Hg^+, Tl^+, Lu^+) with optical frequency splittings. Some species (e.g., Ba^+, Lu^+, Yb^+) have sufficiently long D or F metastable excited state lifetimes to host qubits in their hyperfine or Zeeman levels with radiofrequency/microwave splittings.

In any of these systems, we label the two relevant qubit states as $|\downarrow\rangle \equiv |\downarrow_z\rangle$ and $|\uparrow\rangle \equiv |\uparrow_z\rangle$, eigenstates of the Pauli operator σ_z separated by energy $E_\uparrow - E_\downarrow = \hbar\omega_0$. In the transverse bases of the Bloch sphere, we define by convention the eigenstates of σ_x as

$$|\downarrow_x\rangle \equiv \frac{|\downarrow\rangle - |\uparrow\rangle}{\sqrt{2}} \tag{1}$$

$$|\uparrow_x\rangle \equiv \frac{|\downarrow\rangle + |\uparrow\rangle}{\sqrt{2}}, \tag{2}$$

and the eigenstates of σ_y as

$$|\downarrow_y\rangle \equiv \frac{|\downarrow\rangle + i\,|\uparrow\rangle}{\sqrt{2}} \tag{3}$$

$$|\uparrow_y\rangle \equiv \frac{i\,|\downarrow\rangle + |\uparrow\rangle}{\sqrt{2}}. \tag{4}$$

A typical quantum operation in the ion trap system is comprised of three sequential steps: initialization, interaction, and measurement, as depicted in Fig. 1. The qubits are initialized through an optical pumping process that prepares each qubit in a nearly pure quantum state [1]. By applying resonant laser radiation that couples the qubit states to appropriate short-lived excited states, each qubit can be initialized with $> 99.9\%$ state purity in a few microseconds. This relies on appropriate selection rules for the excited states and also the frequency splitting of the qubit states themselves (Fig. 1a). Laser cooling can prepare the motional states of the ions to near the ground state of harmonic motion [2], which is important for the control of the qubit interactions as detailed below.

Each qubit can be coherently manipulated by driving the atomic ions with external fields that couple the qubit states. This can be accomplished by resonantly driving the energy levels with appropriate radiation at frequency ω_0, or in Fig. 1b, this is depicted as a two-field Raman process, with a beatnote of two optical fields at ω_0 driving the qubit (this will be assumed throughout unless otherwise indicated). This coherent coupling can also drive motional sideband transitions [2] that couple the qubit to the motion of the ion. For multiple ions, this can be used to generate qubit couplings mediated by the Coulomb interaction, described in more detail below [3]. These external fields provide exquisite control over the effective qubit interaction graph, with the ability to gate the interaction, program different forms of the interaction strength and range, and even reconfigure the interaction graph topology for didgital quantum gates or analog quantum simulation applications.

At the end of the coherent quantum operation, the qubits are measured by applying resonant laser radiation that couples one of the two qubit states to a short-lived excited state through a cycling transition and detecting the resulting fluorescence [4, 5, 6]. This is depicted in Fig. 1c, where we take the $|\uparrow\rangle$ or "bright" state as fluorescing and the $|\downarrow\rangle$ or "dark" state as not fluorescing. Even though the photon collection efficiency may be small (typically less than 1%), the effective qubit detection efficiency can be well above 99% owing to the low probability of leaving the fluorescence cycle or having the other (dark) state entering the cycle [7, 8, 9, 10, 11]. In order to detect the qubits in other bases in the Bloch sphere (σ_x or σ_y), previous to fluorescence measurement the qubits are coherently rotated by polar angle $\pi/2$ along the y or x axis of the Bloch sphere, respectively.

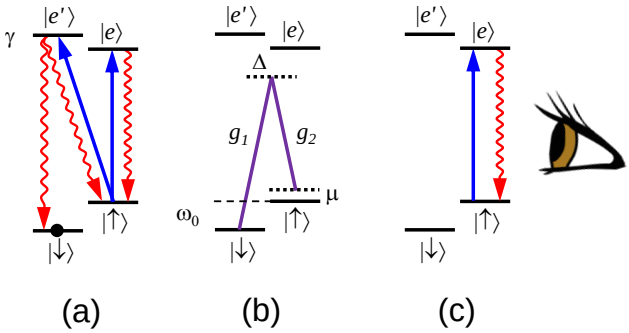

Figure 1: Reduced energy level diagram of a single atomic ion with qubit levels $|\downarrow\rangle$ and $|\uparrow\rangle$. A typical quantum process is comprised of three steps: **(a)** Resonant radiation (blue lines) connects one of the two qubit states to a pair of excited state levels (linewidth γ) and optically pumps each qubit to the $|\downarrow\rangle$ state through spontaneous emission (wavy dotted lines). Here we assume that the excited state $|e\rangle$ couples only to $|\uparrow\rangle$ while the other excited state $|e'\rangle$ couples to both qubit states. **(b)** For ground-state (e.g., Zeeman or hyperfine) defined qubits separated by frequency ω_0, two tones of off-resonant radiation (purple lines) can drive stimulated Raman transitions between the qubit states. The two beams have resonant Rabi frequencies $g_{1,2}$ connecting respective qubit states to excited states and are detuned by $\Delta \gg \gamma$, and have a difference frequency (beatnote) detuned from the qubit resonance by μ. The system can also be driven directly by radiofrequency, microwave signals, a single laser tone. **(c)** Resonant radiation drives the $|\uparrow\rangle \leftrightarrow |e\rangle$ cycling transition, causes the $|\uparrow\rangle$ state to fluoresce strongly (wavy dotted lines), while the $|\downarrow\rangle$ state is far from resonance and therefore dark. This allows the near-perfect detection of the qubit state by the collection of fluorescence.

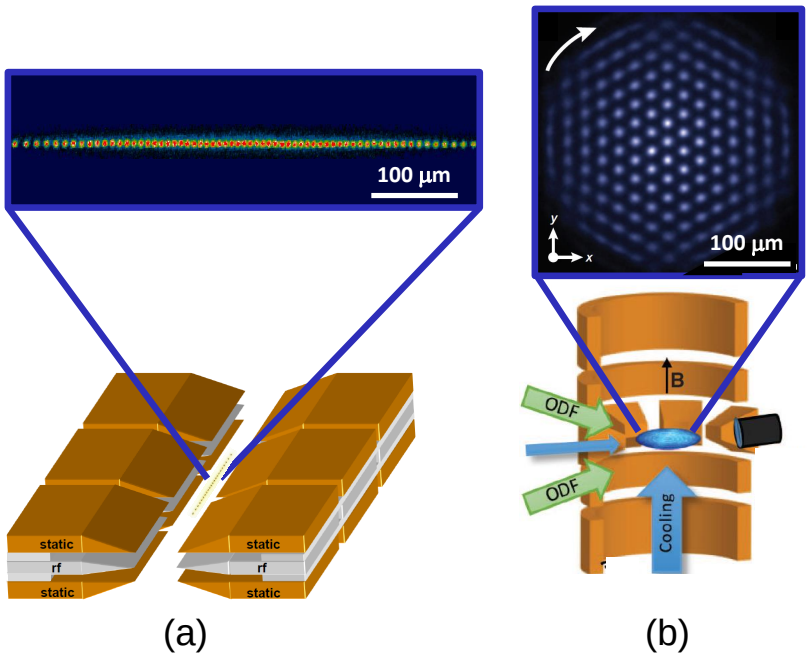

Figure 2: (a) Radiofrequency (rf) linear trap used to prepare a 1D crystal of atomic ions. The geometry in this trap has three layers of electrodes, with the central layer (gray) carrying rf potentials to generate a 2D quadrupole along the axis of the trap. Static electrodes (gold) confine the ions along the axis of the trap. For sufficiently strong transverse confinement, the ions form a linear crystal along the trap axis, with an image of 64 ions shown above with characteristic spacing 5 μm for $^{171}\mathrm{Yb}^{+}$ ions. From [19]. (b) Penning trap used to prepare a 2D crystal of atomic ions. The gold electrodes provide a static quadrupole field that confines the ions vertically, and the vertical magnetic field stabilizes their orbits in the transverse plane. For sufficiently strong axial confinement, the lowest energy configuration of the ions is a single plane triangular lattice that undergoes rigid body rotation, with an image of ~ 200 $^{9}\mathrm{Be}^{+}$ ions shown above with a characteristic spacing of 20 μm. From [18].

1.2 Coulomb-Collective Motion of Trapped Ion Crystals

Atomic ions can be confined in free space with electromagnetic fields supplied by nearby electrodes. Two types of ion traps are conventionally used for quantum information processing: the linear radiofrequency (rf) trap and the Penning trap. The linear rf trap (Fig 2a) [12] juxtaposes a static axial confining potential with a two-dimensional rf quadrupole potential that provides a time-averaged or ponderomotive transverse confinement potential [13, 14]. The trap anisotropy is typically adjusted so that the static axial confinement is much weaker than the transverse confinement so that laser-cooled ions reside on the axis of the trap where the rf fields are null, resulting in a one-dimensional chain of trapped ion qubits. A harmonic axial confinement potential results in an anisotropic linear ion spacing [15], but they can be made nearly equidistant by applying an appropriate quartic axial confining potential [16]. The Penning trap (Fig 2b) juxtaposes a uniform axial magnetic field with a static axial confining potential, and the transverse confinement is provided by the $\mathbf{E} \times \mathbf{B}$ drift toward the axis [17, 18]. Here, the trap anisotropy is typically adjusted so that the ions form a two-dimensional crystal perpendicular to and rotating about the axis. Both traps can be modified to support other types of crystals in any number of spatial dimensions, but the quantum simulations reviewed here are either 1-D chains in rf traps or 2-D crystals in Penning traps. (It should be noted that the dimensionality of the qubit interaction graph does not necessarily follow that of the spatial arrangement of qubits, as described below.)

Ions are typically loaded into traps by generating neutral atoms of the desired element and ionizing the atoms once in the trapping volume via electron bombardment or photoionization. Ion trap depths are usually much larger than room temperature, so rare collisions with background gas do not necessarily eject the ion from the trap, but they can temporarily break up the crystal and scramble the atomic ions in space. Under typical ultra-high-vacuum conditions, these interruptions occur roughly once per hour per ion [20], but cryogenic vacuum chambers can reduce the collision rate by orders of magnitude, where the trapped ions can be undisturbed for weeks or longer between collisions.

When atomic ions are laser-cooled and localized well below their mean spacing, they form a stable crystal, with the Coulomb repulsion balancing the external confinement force. Typical spacings between adjacent ions in trapped ion crystals are $\sim 3-20$ μm, depending on the ion mass, number of ions in the crystal, the characteristic dimensions of the electrodes, and the applied potential values. The equilibrium positions of ions in the crystal can be calculated numerically [15, 21, 22]. The motion of the ions away from their equilibrium positions is well-described by harmonic normal modes of oscillation (phonon modes), with frequencies in the range $\omega_m/2\pi \sim 0.1-10$ MHz. The thermal motion of laser-cooled ions and also the driven motion by external forces is typically at the $10-100$ nm scale. This is much smaller than the inter-ion spacing, so nonlinearities to the phonon modes [23] can be safely neglected and the harmonic approximation to the phonon modes is justified. Calculations of the phonon mode frequencies and normal mode eigenfunctions follow straighforwardly from the calculated ion spacings [15, 21, 22].

For the systems described here, we consider the motion along a single spatial dimension labeled X. We write the $X-$component of position of the ith ion as $\hat{X}_i = \bar{X}_i + \hat{x}_i$, separating the mean (stationary) position $\bar{X}_i$ of the ith ion from the small harmonic oscillations described by the quantum position operator $\hat{x}_i$. The motion of ions in the crystal is tightly coupled by the Coulomb interaction, so it is natural to express the position operator in terms of the $m = 1 \ldots N$ normal (phonon) modes, $\hat{x}_i = \sum_{m=1}^{N} b_{im}\hat{\xi}_m$, where b_{im} is the normal mode transformation matrix, with $\sum_i b_{im}b_{in} = \delta_{nm}$ and $\sum_m b_{im}b_{jm} = \delta_{ij}$. Each phonon mode $\hat{\xi}_m$ oscillates at frequency ω_m, and can be described as a quantum harmonic oscillator with zero-point spatial spread $\xi_m^{(0)} = \sqrt{\hbar/2M\omega_m}$, where M is the mass of a single ion. In the interaction frame for each phonon mode, the position of the ith ion is thus written as

$$\hat{X}_i = \bar{X}_i + \sum_{m=1}^{N} b_{im}\xi_m^{(0)}(a_m^\dagger e^{i\omega_m t} + a_m e^{-i\omega_m t}), \tag{5}$$

where $a_m^\dagger$ and a_m are bosonic raising and lowering operators for each mode, with $[a_m^\dagger, a_n] = \delta_{nm}$.

In general, the structure of transverse phonon modes of a 1D or 2D ion crystal has the center-of-mass mode as its highest frequency, with the lowest frequency corresponding to zig-zag motion where adjacent ions move in opposite directions, as shown in Fig. 3. The bandwidth of the modes can be controlled by tuning the spatial anisotropy of the trap.

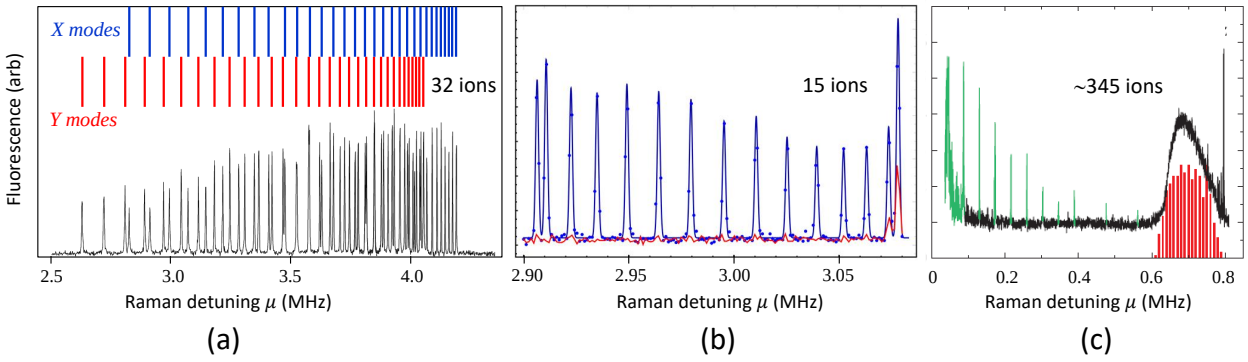

Figure 3: Raman sideband spectra of the transverse motion of trapped atomic ion crystals. The spectrum is measured by preparing all of the ions in state $|\downarrow\rangle$ and driving them with global Raman laser beams with beatnote detuning μ from the qubit resonance and measuring the total fluorescence of the chain. (a) 32 trapped $^{171}\mathrm{Yb}^+$atomic ions in a linear chain (see Fig. 2a). Here, the Raman excitation is sensitive to both X and Y principal axes of transverse motion, and the theoretical position of both sets of 32 modes are indicated at top in blue and red. The highest frequency sidebands correspond to center-of-mass modes at 4.19 MHz for the X direction and 4.05 MHz for the Y direction. (b) Upper (blue) and lower (red) sideband spectra of 15 ions held in an anharmonic trap that produces near-equal spatial spacings. (c) Measured (black) and calculated (red) sideband spectrum for 2D crystal of 345 ± 25 $^9\mathrm{Be}^+$ions in a Penning trap (see Fig. 2b) with rotation frequency 43.2 kHz. As in the linear chain, the highest frequency sideband corresponds to center-of-mass motion. Features at the rotation frequency and its harmonics harmonics (green) are due to residual couplings to in-plane degrees of freedom from imperfect beam alignment [21].

2 Interaction with Near-Resonant Fields

The lab frame Hamiltonian for ions illumated with near-resonant radiation tuned to frequency $\omega_L = \omega_0 + \mu_i$ is given by

$$H_{\rm lab} = \frac{\omega_0}{2}\sum_{i=1}^{N}\sigma_z^i + \sum_{m=1}^{N}\omega_m \hat{a}_m^\dagger \hat{a}_m - \sum_{i=1}^{N}\hat{\mathbf{d}}_i \cdot \mathbf{E}(\hat{X}_i). \tag{6}$$

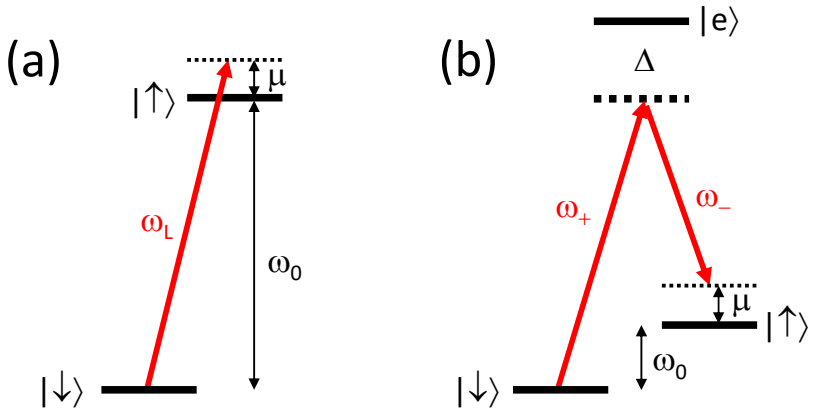

Figure 4: Qubit levels $|\downarrow\rangle$ and $|\uparrow\rangle$ in a single atomic ion, separated by energy $\hbar\omega_0$ and coupled by (optical) fields that drive qubit at frequency $\omega_0 + \mu$. (a) Direct (optical) transition driven by field at frequency ω_L. (b) Two-beam Raman transition with phase coherent fields that each virtually couple respective qubit levels with excited state $|e\rangle$ and produce beat note at frequency $\omega_+ - \omega_-$.

We assume a running wave field illuminating the ions at position $\hat{X}_i$ with field $\mathbf{E}_i(\hat{X}_i) = \mathbf{E}_{i0}\cos(k\hat{X}_i - \omega_L t - \phi_i)$. The field is assumed to be appropriately polarized to couple the two qubit levels and we write $-\hat{\mathbf{d}}_i \cdot \mathbf{E}_{i0} = \Omega_i(\sigma_+^i + \sigma_-^i)$, where Ω_i is the resonant Rabi frequency on ion i. Transforming to the interaction frame and ignoring fast rotating terms at $e^{\pm i(\omega_L+\omega_0)t}$ (rotating wave approximation for $\omega_L, \omega_0 \gg \Omega_i$), we find

$$H = \sum_{i=1}^{N}\frac{\Omega_i}{2}\left(\sigma_+^i e^{i(k\hat{X}_i - \mu_i t - \phi_i)} + \sigma_-^i e^{-i(k\hat{X}_i + \mu_i t - \phi_i)}\right) + s_i\sigma_z^i. \tag{7}$$

The last term is an AC Stark shift of the ith qubit by amount s_i and arises from differential AC Stark shifts between the two qubit levels from the Raman beams. This shift includes the "two-photon" differential Stark shift terms scaled by $(g_1^2 + g_2^2)\omega_0/4\Delta^2$ and summed over each excited state detuned by Δ, where $\omega_0 \ll \Delta$ (see Fig. 1). There are also "four-photon" Stark shifts scaled by $\Omega_i^2/4\mu_i$ and summed over each two-photon Raman resonance detuned by μ, where $\Omega_i \ll \mu_i$. The magnitude of these shifts depends greatly on the atomic energy level structure and light polarization: see [24] for a discussion of Raman-coupled qubits (Fig 1) and [25] for direct optically-coupled qubits. These Stark shifts can be either absorbed into the definition of the qubit energy levels, or used as an effective axial magnetic field for simulations. Below we largely ignore these Stark shifts ($s_i = 0$).

For two-beam Raman transitions between $|\downarrow\rangle$ and $|\uparrow\rangle$, assumed as the default (see Fig 4b), the two beams have wavevectors $\mathbf{k}_\pm$, frequencies $\omega_\pm$ and optical phases $\phi_i^\pm$ where the $\pm$ sign refers to the beam with greater/lesser frequency ($\omega_+ > \omega_-$). We assume the two beams are oriented to have a wavevector difference of $\delta\mathbf{k} = \mathbf{k}_+ - \mathbf{k}_-$, with $\delta k = \delta\mathbf{k}\cdot\hat{\mathbf{X}}$ its projection along the $X-$axis of motion. The Raman beatnote is detuned by frequency $\omega_+ - \omega_- = \omega_0 + \mu_i$ from the resonance of qubit i with beat note phase $\delta\phi_i = \phi_i^+ - \phi_i^-$. In this case, the carrier Hamiltonian is the same as Eq. 10, with $k \to \delta k$, $\phi_i \to \delta\phi_i$ and $\Omega_i = g_1^i g_2^i/2\Delta$, where $g_{1,2}^i$ are the direct (single field) Rabi frequencies of the associated transitions through the excited states, proportional to the respective applied optical electric fields.

Substituting Eq. 5 into Eq. 7, we have

$$H = \sum_{i=1}^{N}\frac{\Omega_i}{2}\sigma_+^i e^{i(\delta k\bar{X}_i - \mu_i t - \delta\phi_i)}\prod_{m=1}^{N} e^{i\eta_{im}(\hat{a}_m^\dagger e^{i\omega_m t} + a_m e^{-i\omega_m t})} + h.c., \tag{8}$$

where Lamb-Dicke parameter $\eta_{i,m} = b_{i,m}\delta k \xi_m^{(0)}$ describes the coupling between ion i and mode m.

This equation is a mess, but by considering a Taylor expansion of the exponential operator, we will find time-stationary terms by setting the detuning μ_i to particular values $\mu_i = \sum_m \ell_m \omega_m$, where ℓ_m are integers. These are just sidebands of order $p = \sum_m |\ell_m|$, and come with prefactor $\eta_{im}^p/p!$. Here we will be interested in just the zeroth and first order terms

$$\prod_{m=1}^{N} e^{i\eta_{im}(\hat{a}_m^\dagger e^{i\omega_m t} + \hat{a}_m e^{-i\omega_m t})} \approx 1 + i\sum_{m=1}^{N} \eta_{im}(\hat{a}_m^\dagger e^{i\omega_m t} + \hat{a}_m e^{-i\omega_m t}). \tag{9}$$

3 Carrier and First Sideband Operations

Next, we specialize to the carrier and the first upper/lower sideband operations, by setting particular values of μ_i in Eq. 8.

3.1 Carrier: $\mu_i = 0$

By tuning the drive to resonance ($\mu_i = 0$), we find

$$H_{\text{car}} = \sum_{i=1}^{N} \frac{\Omega_i}{2} \hat{D}_i^0 \left[\sigma_+^i e^{i(\delta k \bar{X}_i - \mu_i t - \delta\phi_i)} + h.c.\right]. \tag{10}$$

The carrier Debye-Waller operator $\hat{D}_i^0 = \prod_{m=1}^{N} \hat{D}_{im}$ is a product of terms for each spectator mode, where the Debye-Waller operator for ion i on mode m is a function of the phonon number n_m,

$$\hat{D}_{im} = e^{-\eta_{im}^2/2} L_{n_m}(\eta_{im}^2) \approx 1 - \eta_{im}^2\left(n_m + \frac{1}{2}\right) + \frac{\eta_{im}^4}{4}\left(n_m^2 + n_m + \frac{1}{2}\right), \tag{11}$$

where $L_k(x)$ is a Laguerre polynomial of order k. The approximation is the lowest order Lamb-Dicke expansion in $n_m\eta_{im}^2$. The operator $\hat{D}_{im}$ entangles qubit i with motional mode m from Eq. 10 for generic motional states (e.g., thermal), thus resulting in effective decoherence of the qubit. Of course for $\eta_{im} \to 0$ (microwaves or co-propagating Raman transitions with $\delta k \sim 0$), then $\hat{D}_i^0 = \hat{D}_{im} = \hat{1}$.

Ignoring Debye-Waller factors, we find the carrier Hamiltonian reduces to

$$H = \frac{1}{2}\sum_i \Omega_i \sigma_{\beta_i}^i, \tag{12}$$

where

$$\sigma_{\theta_i}^i \equiv \sigma_+^i e^{-i\theta_i} + \sigma_-^i e^{i\theta_i} = \sigma_x^i \cos\theta_i + \sigma_y^i \sin\theta_i \tag{13}$$

is the Pauli spin operator in the xy plane of the Bloch sphere at an angle

$$\beta_i = \phi_i - k\bar{X}_i \qquad \text{for direct transitions (Fig 4a)} \tag{14}$$

$$\beta_i = \delta\phi_i - \delta k\bar{X}_i \qquad \text{for Raman transitions (Fig 4b).} \tag{15}$$

Tuning the Raman laser beat note away from the carrier with $\mu \gg \Omega_i$ generally results in a four-photon AC Stark shift of the qubit levels as discussed above, given by the last term in Eq. (7) [25, 24]. When each qubit is exposed to a unique intensity of light and/or detuning of a single beam, parametrized by s_i, this gives rise to a site-dependent effective Z-phase operation.

3.2 Upper/Blue Sideband: $\mu_i \approx +\omega_m$

By tuning the drive near the upper/blue sideband at $\mu_i = \omega_m + \delta_m$ (detuned by δ_m from mode m), with phase ϕ_i^B,

$$H_{\text{bsb}} = \sum_{i=1}^{N} \frac{\Omega_i}{2} \sum_{m=1}^{N} \hat{D}_{im}^{\text{spec}} \hat{D}_{im}^{B} i\eta_{im} \left[\sigma_+^i \hat{a}_m^\dagger e^{-i\delta_m t} e^{i(\delta k \bar{X}_i - \delta\phi_i^B)} + h.c. \right]. \tag{16}$$

The blue sideband Debye-Waller operator has two components, one for spectator modes $m' \neq m$, $\hat{D}_{im}^{\text{spec}} = \prod_{m' \neq m} \hat{D}_{im}$ (see Eq. 11) and the other for the driven mode

$$\hat{D}_{im}^{B} = e^{-\eta_{im}^2/2} \left[\frac{L_{n_m}^1(\eta_{im}^2)}{n_m + 1} \right] \approx 1 - \eta_{im}^2 \left(\frac{n_m + 1}{2} \right) + \frac{\eta_{im}^4}{12} \left((n_m + 1)^2 + \frac{1}{2} \right), \tag{17}$$

where $L_k^1(x)$ is a first associated Laguerre polynomial of order k. The approximation is the lowest order Lamb-Dicke expansion in $n_m \eta_{im}^2$.

3.3 Lower/Red Sideband: $\mu_i \approx -\omega_m$

By tuning the drive near the lower/red sideband at $\mu_i = -(\omega_m + \delta_m)$ (detuned by δ_m from mode m), with phase ϕ_i^R, we find similarly

$$H_{\text{rsb}} = \sum_{i=1}^{N} \frac{\Omega_i}{2} \sum_{m=1}^{N} \hat{D}_{im}^{\text{spec}} \hat{D}_{im}^{R} i\eta_{im} \left[\sigma_+^i \hat{a}_m e^{+i\delta_m t} e^{i(\delta k \bar{X}_i - \delta\phi_i^R)} + h.c. \right]. \tag{18}$$

The red sideband Debye-Waller operator likewise has two components: one for spectator modes $m' \neq m$, $\hat{D}_{im}^{\text{spec}} = \prod_{m' \neq m} \hat{D}_{im}$ (see Eq. 11) and the other for the driven mode ($n_m \geq 1$)

$$\hat{D}_{im}^{R} = e^{-\eta_{im}^2/2} \left[\frac{L_{n_m-1}^1(\eta_{im}^2)}{n_m} \right] \approx 1 - \eta_{im}^2 \left(\frac{n_m}{2} \right) + \frac{\eta_{im}^4}{12} \left(n_m^2 + \frac{1}{2} \right). \tag{19}$$

3.4 Red + Blue Sideband

When noncopropagating laser beams have bichromatic beat notes at frequencies $\omega_0 \pm \mu_i$ symmetrically detuned from the carrier with $\mu_i \approx \omega_m$, both upper and lower motion-induced sidebands of the normal modes of motion are driven in the ion crystal, giving rise to a spin-dependent force at frequency μ_i [26, 27, 28, 29]. Owing to the symmetry of the detuned beatnotes, the four-photon Stark shift is generally negligible. However, when the bichromatic beat notes are asymmetrically detuned from the carrier by $\omega_0 + \mu_{i+}$ and $\omega_0 - \mu_{i-}$, the effective spin-dependent force occurs at frequency $\mu_i = (\mu_{i+} + \mu_{i-})/2$ and the asymmetry provides a Stark shift that gives rise to an effective uniform axial magnetic field in Eq. (7) with $s_i = \mu_{i+} - \mu_{i-}$.

Under the rotating wave approximation ($\omega_0 \gg \mu_i \gg \Omega_i$) and within the Lamb-Dicke limit, we can add the upper and lower sideband Hamiltonians above, resulting in (ignoring all Debye-Waller factors):

$$H(t) = \frac{1}{2} \sum_{i,m} \eta_{i,m} \Omega_i \sigma_{\theta_i}^i \left[\hat{a}_m^\dagger e^{-i(\delta_{im} t + \psi_i)} + \hat{a}_m e^{i(\delta_{im} t + \psi_i)} \right]. \tag{20}$$

The above expression includes two phases: a "spin phase" θ_i that determines the angle of the ith spin operator in the XY plane of the Bloch sphere that diagonalizes the spin-dependent force; and a "motion phase" ψ_i that determines the

phase of the optical forces (but does not play a role in the effective spin-spin interactions as developed below). These phases depend on the geometry of the bichromatic laser beams and there are two cases written in Eqs. 21-22 [30, 31]. When the upper and lower sideband running wave beat notes propagate in the same direction (δk is the same sign for both), this is termed the "phase-sensitive" geometry. On the other hand, when the upper and lower sideband running waves propagate in opposite directions (opposite sign of δk for the two beat notes), this is called "phase-insensitive." The phases for each configuration are written,

$$\begin{array}{lll} & \text{SPIN PHASE} & \text{MOTION PHASE} \\ \text{PHASE-SENSITIVE} & \theta_i = \left(\frac{\delta\phi_i^B + \delta\phi_i^R}{2}\right) - \delta k\bar{X}_i - \frac{\pi}{2} & \psi_i = \left(\frac{\delta\phi_i^B - \delta\phi_i^R}{2}\right) \end{array} \tag{21}$$

$$\text{PHASE-INSENSITIVE} \quad \theta_i = \left(\frac{\delta\phi_i^B + \delta\phi_i^R}{2}\right) \qquad \psi_i = \left(\frac{\delta\phi_i^B - \delta\phi_i^R}{2}\right) - \delta k\bar{X}_i - \frac{\pi}{2}. \tag{22}$$

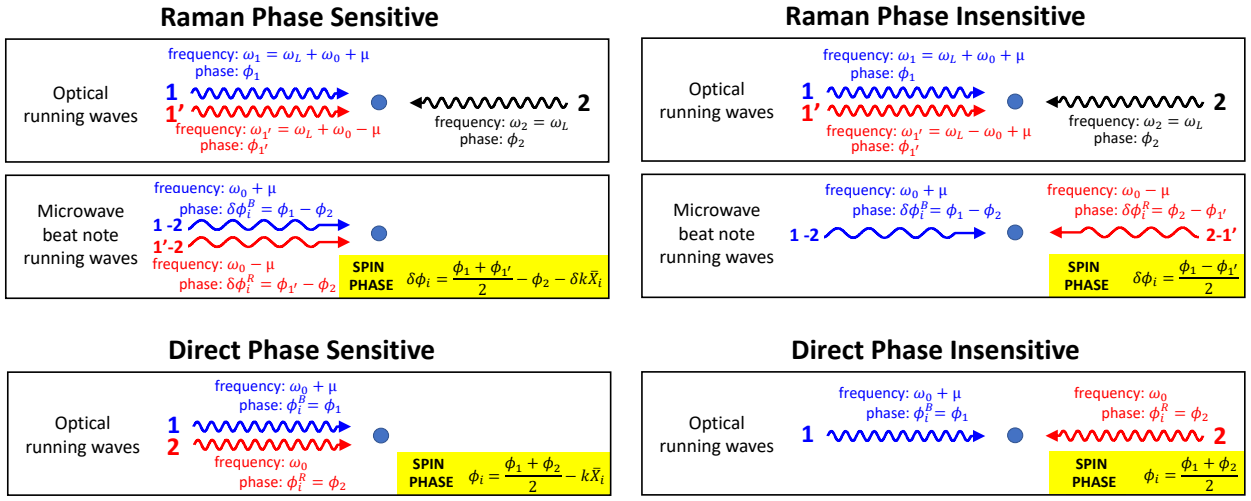

Figure 5: Configurations for driving qubit with bichromatic fields. Top panels are Raman configurations, where beat notes drive the qubit. Bottom pannels are for direct transitions. Note that for Raman geometries, the relative optical phases of the three tones allow for phase insensitivity to both $\delta k\bar{X}_i$ and relative optial paths. But for direct qubit transitions, the spin phase is always phase-sensitive to the sum of the two optical phases.

The sensitivity of the spin phase on $\delta k\bar{X}_i$ has great importance on the practical implementation of spin-spin Hamiltonians. In the phase-sensitive geometry, this dependence may be desired when the phase of other Hamiltonian terms (such as the carrier spin flip operation of Eq. 12) have the same form (see Eq. 15). However, sensitivity to $\delta k\bar{X}_i$ can lead to decoherence if there are drifts in the relative path length of non-copropagating beams or the ion chain along the X-direction. The Phase Insensitive configuration is therefore useful for long simulation evolution times.

We finally note that the phase-insensitive geometry using Raman couplings (Fig. 4b) can remove the spin-phase sensitivity to not only the absolute optical phase of the optical source, but also the relative optical path length difference between the counterpropagating beams, by setting $\delta\phi_i^B = -\delta\phi_i^R$ [30, 31]. The only remaining phase sensitivity is then to the relative optical path length from two tones that can share the same path (see Fig. 5). This is not possible with direct optical upper and lower sideband transitions on qubits with an optical energy splitting (see Fig. 5).

3.5 Mølmer-Sørensen Operation

For either phase configuration of the bicrhomatic red+blue sideband operation, the evolution operator under this Hamiltonian can be written from the Magnus expansion, which terminates after the first two terms [32],

$$U(\tau) = \exp\left[-i\int_0^\tau dt H(t) - \frac{1}{2}\int_0^\tau dt_1 \int_0^{t_1} dt_2 \left[H(t_1), H(t_2)\right]\right] \tag{23}$$

$$= \exp\left[\sum_i \hat{\zeta}_i(\tau)\sigma^i_{\theta_i} - i\sum_{i<j}\chi_{i,j}(\tau)\sigma^i_{\theta_i}\sigma^j_{\theta_i}\right]. \tag{24}$$

The first term of Eq. (24) is a qubit-phonon coupling with operator

$$\hat{\zeta}_i(\tau) = \sum_m \left[\alpha_{i,m}(\tau)a^\dagger_m - \alpha^*_{i,m}(\tau)a_m\right], \tag{25}$$

representing spin-dependent coherent displacements [33, 2] of the mth motional mode through phase space by

$$\alpha_{i,m}(\tau) = -\frac{i}{2}\eta_{i,m}\Omega_i \int_0^\tau dt e^{-i(\delta_{im}t+\psi_i)} = -\frac{\eta_{i,m}\Omega_i e^{-i\psi_i}}{2\delta_{im}}\left(1 - e^{-i\delta_{im}\tau}\right). \tag{26}$$

The second term of Eq. (24) is the key result: a spin-spin or qubit-qubit interaction between ions i and j with coupling strength

$$\chi_{i,j}(\tau) = \Omega_i\Omega_j \sum_m \eta_{i,m}\eta_{j,m}\int_0^\tau dt_1 \int_0^{t_1} dt_2 \sin(\delta_{im}t_1 - \delta_{jm}t_2) \tag{27}$$

$$= \Omega_i\Omega_j \sum_m \frac{\eta_{i,m}\eta_{j,m}}{\delta_{im}\delta_{jm}}\left[\left(\frac{\delta_{im}+\delta_{jm}}{2}\right)\tau - \left(\frac{\sin\delta_{im}\tau + \sin\delta_{jm}\tau}{2}\right)\right] \tag{28}$$

$$= \Omega_i\Omega_j \sum_m \frac{\eta_{i,m}\eta_{j,m}}{\delta_m}\left(\tau - \frac{\sin\delta_m\tau}{\delta_m}\right), \text{ for } \delta_{im} = \delta_m. \tag{29}$$

Fractional corrections to this expression arising from higher-order terms in the Lamb-Dicke expansion leading to Eq. 20 can be shown to be of order $\eta^2_{i,m}\eta^2_{j,m}\bar{n}^2_m$ from Debye-Waller factors above.

3.5.1 Resonant Regime: Digital Gates

In the "resonant" regime [34, 29, 28], the optical beatnote detuning μ is close to one or more normal modes and the qubits become entangled with the motion through the spin-dependent displacements. However, at certain times of the evolution $\alpha_{i,m}(\tau) \approx 0$ for all modes m and the motion nearly decouples from the qubit states, which is useful for applying synchronous entangling quantum logic gates between the qubits. For closely-spaced modes such as the transverse modes, resolving individual modes becomes difficult and may require laser-pulse-shaping techniques [32].

For the case of applying a spin-dependent force to just two ions i and j in the chain, which is common for the execution of entangling two-qubit quantum logic gates, the evolution operator in Eq. 24 reduces to

$$U_{ij}(\tau) = e^{-i\chi_{ij}(\tau)} \left|\uparrow_{\theta_i}\uparrow_{\theta_j}\right\rangle\left\langle\uparrow_{\theta_i}\uparrow_{\theta_j}\right| \prod_m \hat{\mathcal{D}}_m\left[\alpha_{im}(\tau) + \alpha_{jm}(\tau)\right] \tag{30}$$

$$+e^{-i\chi_{ij}(\tau)} \left|\downarrow_{\theta_i}\downarrow_{\theta_j}\right\rangle\left\langle\downarrow_{\theta_i}\downarrow_{\theta_j}\right| \prod_m \hat{\mathcal{D}}_m\left[-\alpha_{im}(\tau) - \alpha_{jm}(\tau)\right] \tag{31}$$

$$+e^{i\chi_{ij}(\tau)} \left|\uparrow_{\theta_i}\downarrow_{\theta_j}\right\rangle\left\langle\uparrow_{\theta_i}\downarrow_{\theta_j}\right| \prod_m \hat{\mathcal{D}}_m\left[\alpha_{im}(\tau) - \alpha_{jm}(\tau)\right] \tag{32}$$

$$+e^{i\chi_{ij}(\tau)} \left|\downarrow_{\theta_i}\uparrow_{\theta_j}\right\rangle\left\langle\downarrow_{\theta_i}\uparrow_{\theta_j}\right| \prod_m \hat{\mathcal{D}}_m\left[-\alpha_{im}(\tau) + \alpha_{jm}(\tau)\right]. \tag{33}$$

In this expression, the spin projection operators are eigenvectors of σ_{θ_i}:

$$|\uparrow_{\theta_i}\rangle = \frac{|\uparrow_i\rangle + e^{-i\theta_i}|\downarrow_i\rangle}{\sqrt{2}}, \tag{34}$$

$$|\downarrow_{\theta_i}\rangle = \frac{|\downarrow_i\rangle - e^{-i\theta_i}|\downarrow_i\rangle}{\sqrt{2}}, \tag{35}$$

with eigenvalues $\langle\uparrow_{\theta_i}|\sigma_{\theta_i}|\uparrow_{\theta_i}\rangle = +1$, $\langle\downarrow_{\theta_i}|\sigma_{\theta_i}|\downarrow_{\theta_i}\rangle = -1$. The coherent displacement operator on mode m is $\hat{\mathcal{D}}_m(\alpha) = e^{\alpha a_m^\dagger - \alpha^* a_m}$ [33]. For full entanglement (as expressive as the CNOT gate), we set $\chi_{ij}(\tau) = \pi/4$.

3.5.2 Dispersive Regime: Analog Simulation

For generating pure spin Hamiltonians, we instead operate in the "dispersive" regime [26, 35], where the optical beatnote frequency is far from each normal mode compared to that mode's sideband Rabi frequency ($|\mu - \omega_m| \gg \eta_{i,m}\Omega_i$). In this case, the phonons are only virtually excited as the displacements become negligible ($|\alpha_{i,m}| \ll 1$), and the result is a fully-connected Ising Hamiltonian from the first (secular) term of Eq. (29):

$$H_{J_\theta} = \sum_{i<j} J_{i,j}\sigma_{\theta_i}^i \sigma_{\theta_j}^j, \tag{36}$$

where the Ising matrix is given by

$$J_{i,j} = \Omega_i\Omega_j \sum_m \frac{\eta_{i,m}\eta_{j,m}}{\delta_m} \tag{37}$$

$$= \Omega_i\Omega_j\omega_{\text{rec}} \sum_m \frac{b_{i,m}b_{j,m}}{2\omega_m}\left(\frac{1}{\delta_{im}} + \frac{1}{\delta_{jm}}\right) \tag{38}$$

$$= \Omega_i\Omega_j\omega_{\text{rec}} \sum_m \frac{b_{i,m}b_{j,m}}{\omega_m\delta_m} \text{ for } \delta_{im} = \delta_m. \tag{39}$$

and $\omega_{\text{rec}} = \hbar(\delta k)^2/2M$ is the recoil frequency associated with the transfer of momentum $\hbar(\delta k)$ to a single ion.

References

[1] William Happer. Optical pumping. *Rev. Mod. Phys.*, 44:169–249, Apr 1972.
[2] D. Leibfried, R. Blatt, C. Monroe, and D. Wineland. Quantum dynamics of single trapped ions. *Rev. Mod. Phys.*, 75:281–324, 2003.
[3] D. Wineland and R. Blatt. Entangled states of trapped atomic ions. *Nature*, 453:1008–1014, 2008.
[4] Warren Nagourney, Jon Sandberg, and Hans Dehmelt. Shelved optical electron amplifier: Observation of quantum jumps. *Phys. Rev. Lett.*, 56:2797–2799, 1986.
[5] Th. Sauter, W. Neuhauser, R. Blatt, and P. E. Toschek. Observation of quantum jumps. *Phys. Rev. Lett.*, 57:1696–1698, 1986.
[6] J. C. Bergquist, Randall G. Hulet, Wayne M. Itano, and D. J. Wineland. Observation of quantum jumps in a single atom. *Phys. Rev. Lett.*, 57:1699–1702, 1986.
[7] M. Acton, K.-A. Brickman, P. C. Haljan, P. J. Lee, L. Deslauriers, and C. Monroe. Near-perfect simultaneous measurement of a qubit register. *Quantum Inf. Comp.*, 6:465, 2006.
[8] D. B. Hume, T. Rosenband, and D. J. Wineland. High-fidelity adaptive qubit detection through repetitive quantum nondemolition measurements. *Phys. Rev. Lett.*, 99:120502, 2007.
[9] J. Benhelm, G. Kirchmair, C. F. Roos, and R. Blatt. Towards fault-tolerant quantum computing with trapped ions. *Nature Physics*, 4:463–466, 2008.
[10] A. H. Myerson, D. J. Szwer, S. C. Webster, D. T. C. Allcock, M. J. Curtis, G. Imreh, J. A. Sherman, D. N. Stacey, A. M. Steane, and D. M. Lucas. High-fidelity readout of trapped-ion qubits. *Phys. Rev. Lett.*, 100:200502, 2008.
[11] Rachel Noek, Geert Vrijsen, Daniel Gaultney, Emily Mount, Taehyun Kim, Peter Maunz, and Jungsang Kim. High speed, high fidelity detection of an atomic hyperfine qubit. *Opt. Lett.*, 38(22):4735–4738, Nov 2013.
[12] M.G. Raizen, J.M. Gilligan, J.C. Bergquist, W.M. Itano, and D.J. Wineland. Linear trap for high-accuracy spectroscopy of stored ions. *Journal of Modern Optics*, 39(2):233–242, 1992.
[13] Hans Dehmelt. Radiofrequency spectroscopy of stored ions i: Storage. *Adv. At. Mol. Phys.*, 3:53–72, 1967.
[14] Wolfgang Paul. Electromagnetic traps for charged and neutral particles. *Rev. Mod. Phys.*, 62:531–540, 1990.
[15] D. F. V. James. Quantum dynamics of cold trapped ions, with application to quantum computation. *Appl. Phys. B*, 66:181–190, 1998.

[16] G.-D. Lin, S.-L. Zhu, R. Islam, K. Kim, M.-S. Chang, S. Korenblit, C. Monroe, and L.-M. Duan. Large-scale quantum computation in an anharmonic linear ion trap. *EPL (Europhysics Lett.)*, 86(6):60004, 2009.
[17] Lowell S. Brown and Gerald Gabrielse. Geonium theory: Physics of a single electron or ion in a penning trap. *Rev. Mod. Phys.*, 58:233–311, 1986.
[18] Justin G Bohnet, Brian C Sawyer, Joseph W Britton, Michael L Wall, Ana Maria Rey, Michael Foss-Feig, and John J Bollinger. Quantum spin dynamics and entanglement generation with hundreds of trapped ions. *Science*, 352(6291):1297–1301, 2016.
[19] R Islam, E. E. Edwards, K. Kim, S. Korenblit, C. Noh, H. Carmichael, G.-D. Lin, L.-M. Duan, C.-C. Joseph Wang, J. K. Freericks, and C. Monroe. Onset of a quantum phase transition with a trapped ion quantum simulator. *Nature Communications*, 2:377, 2011.
[20] D. J. Wineland, C. Monroe, W. M. Itano, D. Leibfried, B. E. King, and D. M. Meekhof. Experimental issues in coherent quantum-state manipulation of trapped atomic ions. *J. Res. Nat. Inst. Stand. Tech.*, 103:259–328, 1998.
[21] Brian C. Sawyer, Joseph W. Britton, Adam C. Keith, C.-C. Joseph Wang, James K. Freericks, Hermann Uys, Michael J. Biercuk, and John J. Bollinger. Spectroscopy and thermometry of drumhead modes in a mesoscopic trapped-ion crystal using entanglement. *Phys. Rev. Lett.*, 108:213003, 2012.
[22] A Steane. The ion trap quantum information processor. *Applied Physics B*, 64:623–643, 1997.
[23] C. Marquet, F. Schmidt-Kaler, and D.F.V. James. Phonon–phonon interactions due to non-linear effects in a linear ion trap. *Applied Physics B*, 76(3):199–208, Mar 2003.
[24] A. C. Lee, J. Smith, P. Richerme, B. Neyenhuis, P. W. Hess, J. Zhang, and C. Monroe. Engineering large stark shifts for control of individual clock state qubits. *Phys. Rev. A*, 94:042308, Oct 2016.
[25] H. Häffner, S. Gulde, M. Riebe, G. Lancaster, C. Becher, J. Eschner, F. Schmidt-Kaler, and R. Blatt. Precision measurement and compensation of optical stark shifts for an ion-trap quantum processor. *Phys. Rev. Lett.*, 90:143602, Apr 2003.
[26] Anders Sørensen and Klaus Mølmer. Quantum computation with ions in thermal motion. *Phys. Rev. Lett.*, 82(9):1971–1974, 1999.
[27] Klaus Mølmer and Anders Sørensen. Multiparticle entanglement of hot trapped ions. *Phys. Rev. Lett.*, 82(9):1835, 1999.
[28] E. Solano, R. L. de Matos Filho, and N. Zagury. Deterministic bell states and measurement of the motional state of two trapped ions. *Phys. Rev. A*, 59:R2539–R2543, 1999.
[29] G.J. Milburn, S. Schneider, and D.F.V. James. Ion trap quantum computing with warm ions. *Fortschritte der Physik*, 48(9-11):801–810, 2000.
[30] P J Lee, K-A Brickman, L Deslauriers, P C Haljan, L-M Duan, and C Monroe. Phase control of trapped ion quantum gates. *Journal of Optics B: Quantum and Semiclassical Optics*, 7(10):S371, 2005.
[31] P. C. Haljan, K.-A. Brickman, L. Deslauriers, P. J. Lee, and C. Monroe. Spin-dependent forces on trapped ions for phase-stable quantum gates and entangled states of spin and motion. *Phys. Rev. Lett.*, 94:153602, Apr 2005.
[32] Shi-Liang Zhu, C. Monroe, and L.-M. Duan. Trapped ion quantum computation with transverse phonon modes. *Phys. Rev. Lett.*, 97:050505, 2006.
[33] Roy J. Glauber. Coherent and incoherent states of the radiation field. *Phys. Rev.*, 131:2766–2788, Sep 1963.
[34] Anders Sørensen and Klaus Mølmer. Entanglement and quantum computation with ions in thermal motion. *Phys. Rev. A*, 62:022311, Jul 2000.
[35] Diego Porras and J Ignacio Cirac. Effective quantum spin systems with trapped ions. *Phys. Rev. Lett.*, 92(20):207901, 2004.